

That’s No Moon: New Analysis Shows No Evidence for Lunar Companion Orbiting Kepler-1625b

LAURA KREIDBERG,^{1,2} RODRIGO LUGER, AND MEGAN BEDELL

¹*Harvard Society of Fellows, 78 Mount Auburn Street, Cambridge, MA 02138*

²*Harvard-Smithsonian Center for Astrophysics, 60 Garden Street, Cambridge, MA 02138*

Submitted to AJ

ABSTRACT

Observations of the Kepler-1625 system with the Kepler and Hubble Space Telescopes suggested the presence of a candidate exomoon, a Neptune-radius satellite orbiting a long-period Jovian planet. Here we present a reanalysis of the Hubble observations. We find that the transit light curve is well fit with a single orbiting body, and that the addition of a moon does not significantly improve the fit quality. The 3σ upper limit on the moon radius is `FIXME`. `FIXME`: why are we different from TK18? We conclude that `FIXME`, and future follow-up efforts for exomoons should focus on alternative targets.

Keywords: planets and satellites: individual (Kepler-1625b)

1. INTRODUCTION

Moons are abundant in the Solar System, and provide clues to the formation history, evolution, and even habitability of the planets they orbit. The great scientific potential of moons has prompted extensive search for lunar companions in exoplanetary systems (exomoons), and creative development of new search techniques (e.g. Kipping 2009a,b; Kipping et al. 2013; Simon et al. 2010; Peters & Turner 2013; Heller et al. 2014; Noyola et al. 2014; Hippke 2015; Agol et al. 2015; Sengupta & Marley 2016; Vanderburg et al. 2018).

Recently, a potential exomoon candidate was identified in the Kepler-1625 system (Teachey et al. 2018). The host planet, Kepler-1625b has radius consistent with that of Jupiter and an orbital period of 287 days. The first evidence for the exomoon candidate, Kepler-1625b I, came from three transit observations from the *Kepler* primary mission that showed `FIXME` (Teachey et al. 2018)...

2. OBSERVATIONS AND DATA REDUCTION

The Kepler-1625 system was observed with 26 continuous *HST* orbits on 28 - 29 October, 2017 (Program GO 15149: PI: A. Teachey). The observations used the Wide Field Camera 3 (WFC3) G141 grism in staring mode, which fixed the spectrum in a constant position on the detector. At the beginning of the visit, there was a single exposure taken with the F130N filter, which is used to determine the position of the spectral trace. The following exposures used the G141 grism with the `SPARS25`,

`NSAMP=15` readout pattern (exposure time of 290.8 seconds; 9 exposures per orbit). For additional description of the observation design, see Teachey & Kipping (2018).

We reduced the *HST* data using custom software developed in Kreidberg et al. (2014). This software has yielded consistent results with multiple independent pipelines (e.g. Knutson et al. 2014; Spake et al. 2018). We ran our pipeline on the `flt` data product provided by the Space Telescope Science Institute (STScI). The `flt` files are corrected for dark current, bias, and non-linearity, and they are cleaned of cosmic ray hits based on a fit to the up-the-ramp samples. In keeping with previous WFC3 analysis, we discarded the first orbit of data, where the instrument systematics have larger amplitude. We also discard exposures taken during the South Atlantic Anomaly passage (exposures 107, 116, 125, and 126).

To begin the data reduction, we fit the centroid of the direct image with a two-dimensional Gaussian. The centroid position determines the position of the spectral trace, which we calculated using the coefficients provided in the configuration file from STScI: `G141.F130N.V4.32.conf`¹. To process the spectra, we flatfielded the raw data using the spectroscopic flatfield coefficients provided by STScI in `WFC3.IR.G141.flat.2.fits`, following the instructions

¹ available at http://www.stsci.edu/hst/wfc3/analysis/grism_obs/calibrations/wfc3_g141.html

in Section 6 of the aXe User Manual². We then created an extraction box centered on the spectral trace. We varied the height and width of the box in 1-pixel increments to find the window that minimized the root-mean-square (rms) deviation from the best fit to the transit light curve. The best was FIXME.

We reduced the grism exposures with the optimal extraction routine of Horne (1986), which minimizes background noise in the extracted spectrum by weighting pixels that are dominated by the target spectrum more heavily than pixels dominated by the background. The inputs for optimal extraction are the background-subtracted data array, the error array (including photon noise read noise, and uncertainty due to background subtraction), an initial guess for the spectrum and its uncertainty, and a mask array for bad pixels. For the initial guess of the spectrum and its uncertainty, we did a simple box extraction (sum over all rows in the extraction window), and assumed the variance was equal to the box-extracted spectrum (expected for photon noise limit). We measured and subtracted the background from the data array as described in 2.1. For the error array, we used a quadrature sum of the photon noise (the square root of the pixel counts), the read noise (12 photoelectrons for `flt` files; WFC3 Data Handbook³), and the error due to background subtraction (described in 2.1). The initial bad pixel mask included pixels marked with the data quality flag 4 or 512 (dead pixels or blobs).

In brief, optimal extraction is an iterative procedure with the following steps. First, we created a smoothed image by median-filtering each row of the data with a 9-pixel-wide window. We then normalized the smoothed image by dividing each column by its sum, and multiplied it by the best guess spectrum. We compared the smoothed image to the real data and masked outliers in the data that are greater than a threshold σ_{cut} . We then recomputed the best guess spectrum with the new mask and the optimal weights from Horne (1986). The process is iterated until no outliers greater than the threshold remain. This procedure masks any cosmic rays or bad pixels that were missed by the initial `flt` calibration. We tested a range of thresholds ($4 < \sigma_{\text{cut}} < 15$) and found that different σ_{cut} choices did not significantly change the final transit light curve. The data reported in this work use $\sigma_{\text{cut}} = 15$. To create the broadband transit light curve, we sum each spectrum over all wavelengths.

² <http://axe-info.stsci.edu/>

³ <http://www.stsci.edu/hst/wfc3/documents/handbooks/currentDHB/>

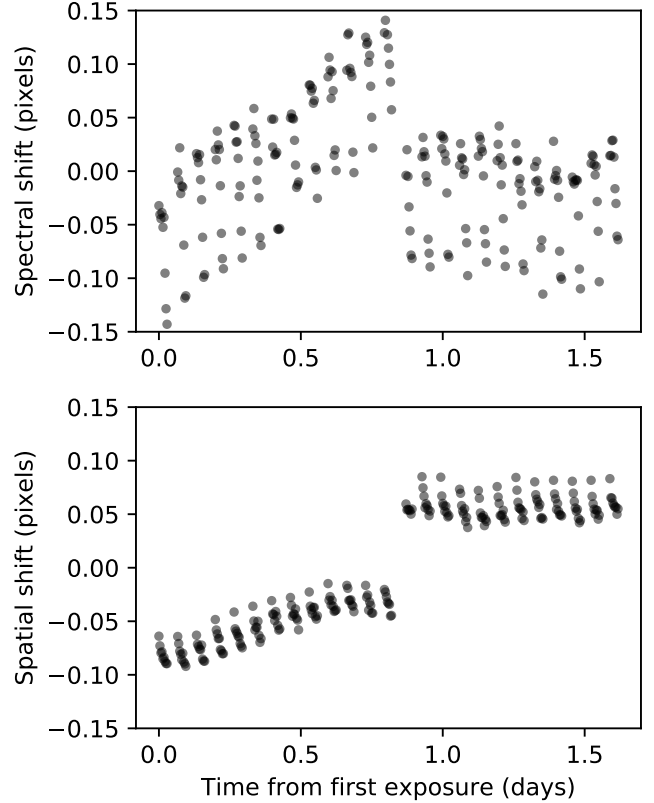


Figure 1. Shift (in pixels) relative to the mean position of the spectrum in the spectral direction (top) and spatial direction (bottom). The largest shift occurs after orbit 14 due to a guide star reacquisition.

2.1. Background Subtraction

The star Kepler-1625 is faint (H mag = 14.0) relative to most other exoplanet host stars observed with WFC3, which makes accurate background subtraction especially important for this target. Moreover, the host star is in a crowded field, so the pixels used to estimate the background must be chosen carefully to avoid contamination from other stars. We identified several uncontaminated regions by eye: $130 < X < 215$ and $6 < Y < 24$; $220 < X < 250$ and $110 < Y < 155$; $6 < X < 47$ and $127 < Y < 141$, where X and Y are pixel numbers in the spectral and spatial direction, respectively (numbering from zero). To estimate the background and its uncertainty for each exposure, we took the median and median absolute deviation (MAD) of the pixel counts in these three regions. The per pixel uncertainty due to background subtraction is 1.4826 times the MAD.

2.2. Pointing Drift Measurement

The position of the spectrum on the detector shifts slightly over time (~ 0.1 pixel/day) due to the space-

craft’s pointing drift. This drift can change the flux measured for the target star: if the spectrum moves onto less sensitive pixels, fewer photoelectrons are recorded. To enable a correction for this effect, we measured the position of the spectrum over time.

To measure shifts in the spatial direction, we first summed each `flt` image over all columns (which we dub the “column sum”). We used the first exposure in the visit as a template, and for each subsequent exposure, we used least-squares minimization to calculate the shift in pixels that minimized the difference between its column sum and the template. The shifts are a fraction of a pixel, so we used the NumPy `interp` routine to do linear interpolation on a sub-pixel scale. The WFC3 point spread function is undersampled, so we convolved each column sum with a 4-pixel-wide Gaussian before the interpolation (following Deming et al. 2013).

To measure the spectral shifts, we repeated this procedure with two differences: (1) we used the optimally extracted spectrum rather than the column sum; and (2) in addition to calculating the best fit shift, we also calculated a best fit normalization factor (a scalar multiple for the whole spectrum), to ensure that our results are not biased by the varying brightness of the host star during the planet’s transit.

Figure 1 shows the best fit shifts. Over the entire 26-orbit visit, the maximum shift is less than 0.2 pixel in the spatial direction and 0.3 pixel in the spectral direction. The largest shift occurs after orbit 14, when the telescope reacquired the guide stars.

3. ANALYSIS

The raw light transit light curve (shown in Figure ??) contains both astrophysical signal and instrument systematic noise, which we model simultaneously.

3.1. Astrophysics Model

For the astrophysics, we used the `planetplanet` package (Luger et al. 2017), a photodynamical code that calculates light curves for multiple occulting bodies orbiting a star. Within `planetplanet`, the orbits are computed with the N-body integrator REBOUND (Rein & Liu 2012). The `planetplanet` model returns the system flux at a specified orbital architecture and time.

In our analysis, we considered two scenarios: a no-moon model and a moon model. The free parameters for the no-moon model were: the stellar radius R_* , the planet radius R_{planet} , the time of central transit t_{planet} , and the planet inclination i . For the moon model, we added a third body with radius R_{moon} , transit time t_{moon} , and orbital period P_{moon} . We allowed the moon period to vary from 1.6 to 260 days. These limits span

the duration of the *HST* observations (so there is one possible moon occultation event), to the orbit at 0.5 the Hill radius, based on the stability limit for prograde moon orbits (Domingos et al. 2006). The Hill radius calculation assumed the planet and stellar masses are $1 M_{\text{Jup}}$ and $1.37 M_{\odot}$.

The models also had several fixed parameters. For the moon model, we fixed inclination of the moon to 90° to exclude grazing transit scenarios, where the moon radius could be arbitrarily large. We also fixed the moon mass and eccentricity to zero. For both the no-moon and moon models, we fixed the planet’s orbital period to 287.378949 days (Teachey & Kipping 2018). We also fixed the planet eccentricity to zero and the mass to $1 M_{\text{Jup}}$. These choices restrict the orbital FIXME

3.1.1. Stellar Parameters

For both the moon and no-moon scenarios, we used a quadratic stellar limb darkening law and fixed the coefficients to the prediction for a 5700 K, solar metallicity PHOENIX model from Espinoza & Jordán (2015); $u_1, u_2 = [0.216, 0.183]$.

We estimated the host star parameters using the Gaia DR2 parallax (Gaia Collaboration et al. 2016, 2018) along with UBV photometry from Everett et al. (2012) and JHK photometry from 2MASS (Skrutskie et al. 2006). We employed the isochrone python package (Morton 2015) with the Dartmouth isochrone grid (Dotter et al. 2008) to obtain posterior constraints on the stellar parameters. The resulting parameters indicate that Kepler-1625 has stellar mass $1.37^{+0.13}_{-0.16} M_{\odot}$, radius $1.81^{+0.18}_{-0.16} R_{\odot}$, and age $2.8^{+1.6}_{-1.2}$ Gyr. In our analysis, we fixed the stellar mass to the best fit value ($1.37 M_{\odot}$), and used a Gaussian prior on the radius, $R_* \sim N(1.81, 0.17)$.

3.2. Instrument Systematics Model

There are two systematic trends in the data. One is the orbit-long ramp, attributed to charge traps in the detector filling up over the orbit (Zhou et al. 2017). The other is a visit-long trend over multiple orbits, which could be due to shifts in the target star position onto more/less sensitive pixels.

To fit the orbit-long ramp, we used the non-parametric model from Teachey & Kipping (2018), which assigns each of the nine exposures per orbit a normalization constant, c_1, \dots, c_9 . To fit the visit-long trend, we used a linear combination of X and Y position (the shift relative to the mean in the spatial and spectral directions, respectively; shown in Figure 1). In sum, for exposure number i , the systematics model is:

$$S_i = c_j \times (1 + aX_i + bY_i) \quad (1)$$

where a and b , and c_j are free parameters, and $j = i \bmod 9 + 1$ is the exposure number relative to the first exposure in the orbit.

3.3. Light Curve Fits

We fit the raw, broadband transit light curve using the models described above. For comparison, we also fit the raw light curve from [Teachey & Kipping \(2018\)](#). We determined the best fit model parameters with least-squares minimization. We also ran a Markov chain Monte Carlo (MCMC) fit to determine the posterior probability of each parameters. The MCMC used the `emcee` package ([Foreman-Mackey et al. 2013](#)) with 50 walkers and ran for 10^4 steps. We discarded the first 20% of the MCMC chain as burn-in. As a quick test for convergence, we divided the remainder of the chain in half and checked that the results from the first half were consistent with the second half.

4. RESULTS

Figure FIXME shows the best fits.

5. DISCUSSION

We did not find evidence for the exomoon. Why are we different from Teachey and Kipping?

Dan Foreman-Mackey

The HST data presented in this paper were obtained from the Mikulski Archive for Space Telescopes (MAST). STScI is operated by the Association of Universities for Research in Astronomy, Inc., under NASA contract NAS5-26555. Support for MAST for non-HST data is provided by the NASA Office of Space Science via grant NNX13AC07G and by other grants and contracts. We also use data from the European Space Agency (ESA) mission *Gaia* (<https://www.cosmos.esa.int/gaia>), processed by the *Gaia* Data Processing and Analysis Consortium (DPAC, <https://www.cosmos.esa.int/web/gaia/dpac/consortium>). Funding for the DPAC has been provided by national institutions, in particular the institutions participating in the *Gaia* Multilateral Agreement. We also use data products from the Two Micron All Sky Survey, which is a joint project of the University of Massachusetts and the Infrared Processing and Analysis Center/California Institute of Technology, funded by the National Aeronautics and Space Administration and the National Science Foundation. This research has made use of the SIMBAD database, operated at CDS, Strasbourg, France; the REBOUND integrator package ([Rein & Liu 2012](#)); the NumPy package ([Van Der Walt et al. 2011](#)); and NASA’s Astrophysics Data System.

REFERENCES

- Agol, E., Jansen, T., Lacy, B., Robinson, T. D., & Meadows, V. 2015, *ApJ*, 812, 5, doi: [10.1088/0004-637X/812/1/5](https://doi.org/10.1088/0004-637X/812/1/5)
- Deming, D., Wilkins, A., McCullough, P., et al. 2013, *ApJ*, 774, 95, doi: [10.1088/0004-637X/774/2/95](https://doi.org/10.1088/0004-637X/774/2/95)
- Domingos, R. C., Winter, O. C., & Yokoyama, T. 2006, *MNRAS*, 373, 1227, doi: [10.1111/j.1365-2966.2006.11104.x](https://doi.org/10.1111/j.1365-2966.2006.11104.x)
- Dotter, A., Chaboyer, B., Jevremović, D., et al. 2008, *ApJS*, 178, 89, doi: [10.1086/589654](https://doi.org/10.1086/589654)
- Espinoza, N., & Jordán, A. 2015, *MNRAS*, 450, 1879, doi: [10.1093/mnras/stv744](https://doi.org/10.1093/mnras/stv744)
- Everett, M. E., Howell, S. B., & Kinemuchi, K. 2012, *Publications of the Astronomical Society of the Pacific*, 124, 316, doi: [10.1086/665529](https://doi.org/10.1086/665529)
- Foreman-Mackey, D., Hogg, D. W., Lang, D., & Goodman, J. 2013, *PASP*, 125, 306, doi: [10.1086/670067](https://doi.org/10.1086/670067)
- Gaia Collaboration, Prusti, T., de Bruijne, J. H. J., et al. 2016, *A&A*, 595, A1, doi: [10.1051/0004-6361/201629272](https://doi.org/10.1051/0004-6361/201629272)
- Gaia Collaboration, Brown, A. G. A., Vallenari, A., et al. 2018, *A&A*, 616, A1, doi: [10.1051/0004-6361/201833051](https://doi.org/10.1051/0004-6361/201833051)
- Heller, R., Williams, D., Kipping, D., et al. 2014, *Astrobiology*, 14, 798, doi: [10.1089/ast.2014.1147](https://doi.org/10.1089/ast.2014.1147)
- Hippke, M. 2015, *ApJ*, 806, 51, doi: [10.1088/0004-637X/806/1/51](https://doi.org/10.1088/0004-637X/806/1/51)
- Horne, K. 1986, *PASP*, 98, 609, doi: [10.1086/131801](https://doi.org/10.1086/131801)
- Kipping, D. M. 2009a, *MNRAS*, 392, 181, doi: [10.1111/j.1365-2966.2008.13999.x](https://doi.org/10.1111/j.1365-2966.2008.13999.x)
- . 2009b, *MNRAS*, 396, 1797, doi: [10.1111/j.1365-2966.2009.14869.x](https://doi.org/10.1111/j.1365-2966.2009.14869.x)
- Kipping, D. M., Hartman, J., Buchhave, L. A., et al. 2013, *ApJ*, 770, 101, doi: [10.1088/0004-637X/770/2/101](https://doi.org/10.1088/0004-637X/770/2/101)
- Knutson, H. A., Dragomir, D., Kreidberg, L., et al. 2014, *ApJ*, 794, 155, doi: [10.1088/0004-637X/794/2/155](https://doi.org/10.1088/0004-637X/794/2/155)
- Kreidberg, L., Bean, J. L., Désert, J.-M., et al. 2014, *Nature*, 505, 69, doi: [10.1038/nature12888](https://doi.org/10.1038/nature12888)
- Luger, R., Lustig-Yaeger, J., & Agol, E. 2017, *ApJ*, 851, 94, doi: [10.3847/1538-4357/aa9c43](https://doi.org/10.3847/1538-4357/aa9c43)
- Morton, T. D. 2015, isochrones: Stellar model grid package, *Astrophysics Source Code Library*, <http://ascl.net/1503.010>

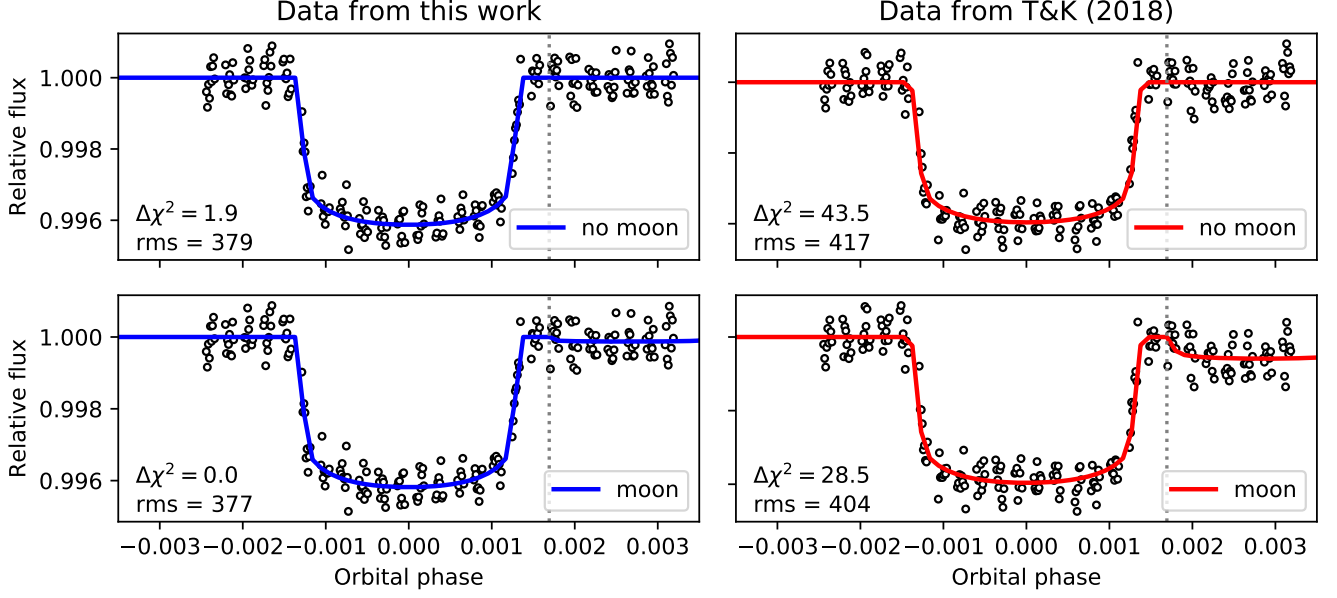


Figure 2. Best fit models compared to transit light curves from this work (left) and from TK18 (right). The top panel shows the best fit no-moon model (blue), and the bottom shows the best fit moon model (red). The lower left of each panel indicates the fit rms (in ppm) and the $\Delta\chi^2$ relative to the overall best fit (data reduction from this work, moon model). The dotted gray line marks the possible moon ingress identified by TK18.

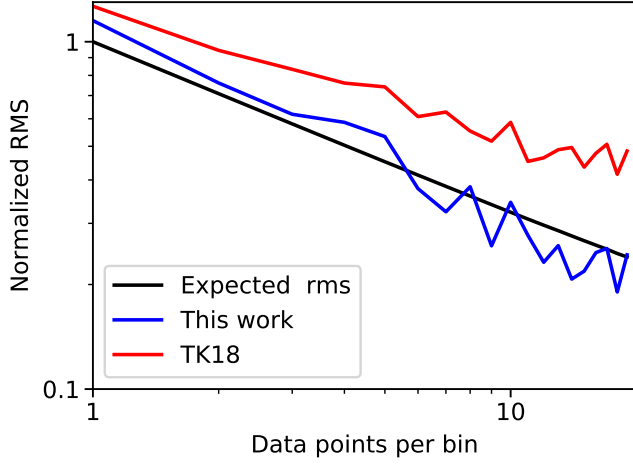


Figure 3. Light curve rms versus bin size for the best fit no-moon model. The fit to data from this work (blue line) agrees well with the expected photon-limited, \sqrt{N} decrease in rms with bin size (black line). The TK18 rms (red line) ranges from 1.3 – 2 \times the photon limit for bin sizes of 1 to 20 data points. The increase in relative rms for larger bin sizes indicates that time-correlated noise is present in the TK18 data.

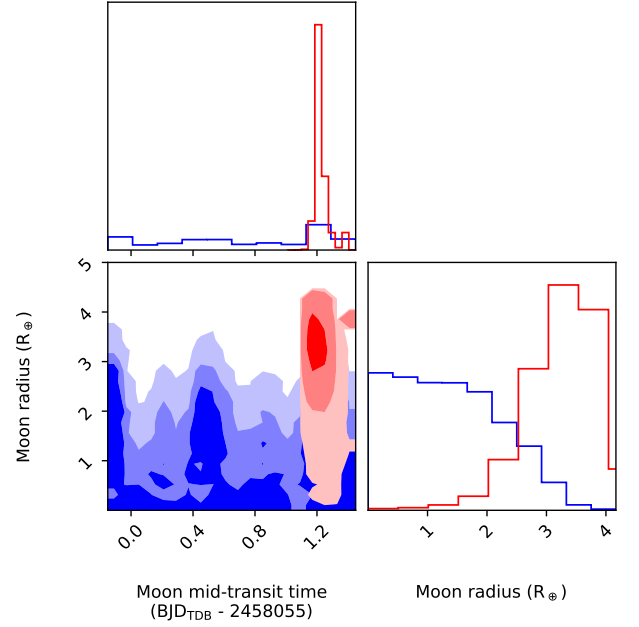


Figure 4. Posterior distributions for the moon radius and time of central transit. Blue = this work; red = our analysis of TK18 data.

Noyola, J. P., Satyal, S., & Musielak, Z. E. 2014, *ApJ*, 791, 25, doi: [10.1088/0004-637X/791/1/25](https://doi.org/10.1088/0004-637X/791/1/25)

Peters, M. A., & Turner, E. L. 2013, *ApJ*, 769, 98, doi: [10.1088/0004-637X/769/2/98](https://doi.org/10.1088/0004-637X/769/2/98)

Rein, H., & Liu, S.-F. 2012, *A&A*, 537, A128, doi: [10.1051/0004-6361/201118085](https://doi.org/10.1051/0004-6361/201118085)

Sengupta, S., & Marley, M. S. 2016, *ApJ*, 824, 76, doi: [10.3847/0004-637X/824/2/76](https://doi.org/10.3847/0004-637X/824/2/76)

- Simon, A. E., Szabó, G. M., Sztatmáry, K., & Kiss, L. L. 2010, MNRAS, 406, 2038, doi: [10.1111/j.1365-2966.2010.16818.x](https://doi.org/10.1111/j.1365-2966.2010.16818.x)
- Skrutskie, M. F., Cutri, R. M., Stiening, R., et al. 2006, AJ, 131, 1163, doi: [10.1086/498708](https://doi.org/10.1086/498708)
- Spake, J. J., Sing, D. K., Evans, T. M., et al. 2018, Nature, 557, 68, doi: [10.1038/s41586-018-0067-5](https://doi.org/10.1038/s41586-018-0067-5)
- Teachey, A., & Kipping, D. M. 2018, Science Advances, 4, eaav1784, doi: [10.1126/sciadv.aav1784](https://doi.org/10.1126/sciadv.aav1784)
- Teachey, A., Kipping, D. M., & Schmitt, A. R. 2018, AJ, 155, 36, doi: [10.3847/1538-3881/aa93f2](https://doi.org/10.3847/1538-3881/aa93f2)
- Van Der Walt, S., Colbert, S. C., & Varoquaux, G. 2011, Computing in Science & Engineering, 13, 22
- Vanderburg, A., Rappaport, S. A., & Mayo, A. W. 2018, AJ, 156, 184, doi: [10.3847/1538-3881/aae0fc](https://doi.org/10.3847/1538-3881/aae0fc)
- Zhou, Y., Apai, D., Lew, B. W. P., & Schneider, G. 2017, AJ, 153, 243, doi: [10.3847/1538-3881/aa6481](https://doi.org/10.3847/1538-3881/aa6481)